

Infrared interferometric three-dimensional diagnosis of the atmospheric dynamics of the AGB star R Dor with VLT/AMBER*

KEIICHI OHNAKA,¹ GERD WEIGELT,² AND KARL-HEINZ HOFMANN²

¹*Instituto de Astronomía, Universidad Católica del Norte
Avenida Angamos 0610, Antofagasta, Chile*

²*Max-Planck-Institut für Radioastronomie
Auf dem Hügel 69, 53121 Bonn, Germany*

(Received; Revised; Accepted)

Submitted to ApJ

ABSTRACT

The mechanism of mass loss in late evolutionary stages of low- and intermediate-mass stars is not yet well understood. Therefore, it is crucial to study the dynamics of the region within a few R_* , where the wind acceleration is considered to take place. We present three-dimensional diagnosis of the atmospheric dynamics of the closest asymptotic giant branch (AGB) star R Dor from the low photospheric layers to the extended outer atmosphere—for the first time for a star other than the Sun. The images reconstructed with a spatial resolution of 6.8 mas—seven times finer than the star’s angular diameter of 51.2 mas in the continuum—using the AMBER instrument at the Very Large Telescope Interferometer show a large, bright region over the surface of the star and an extended atmosphere. The velocity-field maps over the star’s surface and atmosphere obtained from the Mg and H₂O lines near 2.3 μm forming at atmospheric heights below $\sim 1.5 R_*$ show little systematic motion beyond the measurement uncertainty of 1.7 km s^{−1}. In marked contrast, the velocity-field map obtained from the CO first overtone lines reveals systematic outward motion at 7–15 km s^{−1} in the extended outer atmosphere at a height of $\sim 1.8 R_*$. Given the detection of dust formation at $\sim 1.5 R_*$, the strong acceleration of material between ~ 1.5 and $1.8 R_*$ may be caused by the radiation pressure on dust grains. However, we cannot yet exclude the possibility that the outward motion may be intermittent, caused by ballistic motion due to convection and/or pulsation.

Keywords: stars: imaging — stars: AGB and post-AGB — stars: atmospheres — stars: mass-loss — techniques: high angular resolution — techniques: interferometric

1. INTRODUCTION

Mass loss in cool evolved stars—stars in the red giant branch (RGB) and asymptotic giant branch (AGB) as well as red supergiants—affects not only the stellar evolution but also the chemical enrichment of galaxies. Despite such importance, the mass-loss mechanism in cool evolved stars is a long-standing problem over half

a century since the discovery of the mass outflow in the red supergiant α Her by Deutsch (1956). In case of AGB stars, it is often argued that the levitation of the atmosphere by pulsation leads to dust formation, and the radiation pressure on dust grains may drive slow but dense stellar winds (e.g., Höfner & Olofsson 2018). In case of oxygen-rich AGB stars, the latest theoretical models suggest that scattering—instead of absorption—of stellar photons by large (a few 0.1 μm), transparent grains may be the driving force (Höfner 2008; Höfner et al. 2016).

To improve our understanding of the mass-loss mechanism, it is crucial to study the region within a few R_* , where the wind acceleration is considered to

Corresponding author: Keiichi Ohnaka
k1.ohnaka@gmail.com

* Based on AMBER observations made with the Very Large Telescope and Very Large Telescope Interferometer of the European Southern Observatory. Program ID: 092.D-0456(A), 092.D-0465(A/B)

take place. Given that even the largest angular diameter of nearby AGB stars is mere 50 mas (that of R Dor, the target of the present paper), we need milliarcsecond spatial resolution to resolve the key region. Optical and infrared interferometric techniques enable us to spatially resolve not only the extended atmosphere but also inhomogeneous surface structures in AGB stars (e.g., Ragland et al. 2008; Lacour et al. 2009; Le Bouquin et al. 2009; Wittkowski et al. 2017; Paladini et al. 2018). Some of the high-spatial resolution images reveal the presence of inhomogeneous molecular outer atmospheres extending out to a few R_* .

The dust formation region close to the star has also been spatially resolved. Optical long-baseline interferometric polarimetric observations of oxygen-rich AGB stars by Ireland et al. (2005) suggest the scattering of stellar light by dust forming closer than about $3 R_*$. The near-infrared aperture-masking experiments of Norris et al. (2012) show the presence of $\sim 0.3 \mu\text{m}$ -sized transparent grains at $\sim 1.5 R_*$ in three AGB stars, including the target of the present paper R Dor. More recently, visible polarimetric imaging observations have revealed the formation of clumpy dust clouds around several oxygen-rich AGB stars (Khouri et al. 2016, 2018; Ohnaka et al. 2016, 2017a; Adam & Ohnaka 2019). In particular, the polarimetric images and the modeling of the nearby, well-studied AGB stars R Dor and W Hya (Khouri et al. 2016; Ohnaka et al. 2016, 2017a) show that dust forms as close as at $\sim 1.5 R_*$, consistent with the results of Norris et al. (2012).

It is of paramount importance to study the dynamics of the extended atmosphere for clarifying the mechanism responsible for the stellar wind acceleration. Detailed spectroscopic analyses of near-infrared atomic and molecular lines show distinct gas motion in the photospheric layers and the extended outer atmosphere (e.g., Hinkle & Barnes 1979). Nevertheless, it is not straightforward to ascertain the atmospheric (i.e., geometrical) height of different layers from the spatially unresolved spectroscopic data. Furthermore, the inhomogeneities over the surface and atmosphere seen in the high-spatial resolution images complicate the interpretation. A direct approach is to measure the line-of-sight velocity at each position over the spatially resolved surface and atmosphere of stars. High-spatial and high-spectral resolution infrared interferometric observations of the $2.3 \mu\text{m}$ CO lines enabled us to obtain a two-dimensional map of the line-of-sight velocity over the surface and atmosphere of the red supergiant Antares—for the first time for a star other than the Sun. In the present paper, we extend this approach to three-dimensional diagnosis of the atmospheric dynamics for the AGB star R Dor.

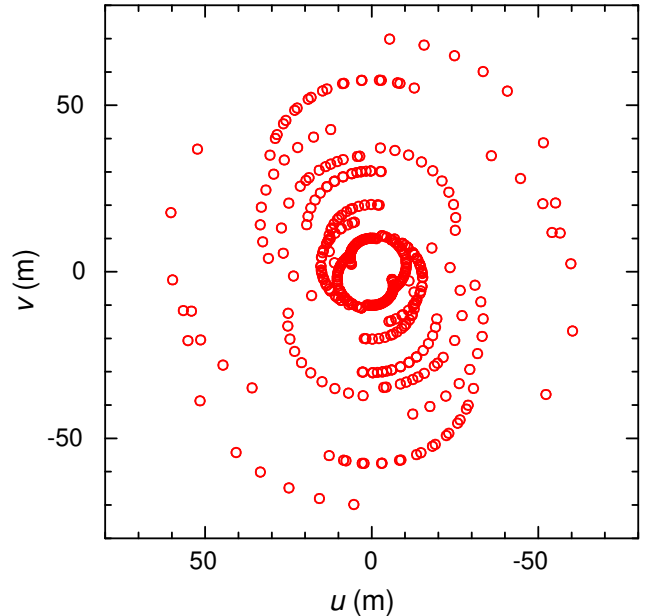


Figure 1. The uv coverage of our VLTI/AMBER observations of R Dor with six different AT configurations.

Our observations and data reduction are summarized in Section 2. The analysis of the reduced data is described in Section 3. We present the results in Section 4 followed by discussion and conclusion in Section 5.

2. OBSERVATIONS AND DATA REDUCTION

2.1. AMBER observations

Our target R Dor is one of the well-studied AGB stars, classified as a semiregular variable of SRB type with a spectral type of M8III (Samus et al. 2017). At a distance of 55 pc (Hipparcos parallax = 18.31 mas, van Leeuwen 2007)¹, it is the closest AGB star. Its extremely high brightness in the infrared and its large angular diameter of 51.2 mas (see Sect. 3.1) provide an excellent opportunity to not only obtain detailed images of its surface and atmosphere but also velocity-field maps (i.e., maps of the line-of-sight velocity) of the atmospheric gas motion.

We observed R Dor with the near-infrared spectro-interferometric instrument AMBER (Petrov et al. 2007) at the Very Large Telescope Interferometer (VLTI) of the European Southern Observatory. Our AMBER observations (Program ID: 092.D-0456(A), 092.D-0465(A/B), P.I.: K. Ohnaka) took place on seven nights allocated within 10 days, 2013 December 1, 2, 6, 7, 8, 9, and 10 UT, thus minimizing possible variations in the

¹ GAIA parallax is not available for R Dor.

structures over the surface and atmosphere. We used six array configurations of the Auxiliary Telescopes (ATs), A1-B2-D0, A1-B2-C1, A1-C1-D0, B2-C1-D0, D0-G1-H0, and G1-H0-I1. The intensive observing program provided a wide baseline coverage from 6.5 to 70 m. This baseline coverage and the southern declination of R Dor (-62°) allowed us to obtain a good uv coverage as shown in Figure 1, with a spatial resolution of 6.8 mas.

The AMBER instrument combines this milliarcsecond angular resolution with a high spectral resolution of up to 12000, which is needed to extract dynamical information over the surface and atmosphere of stars using Doppler shifts of individual spectral lines. We observed the wavelength range between 2.278 and 2.308 μm with the spectral resolution of 12000. In this spectral window, there are strong CO first overtone lines of the $v = 2 - 0$ transition that form in the *extended outer atmosphere* as well as other molecular and atomic lines, such as due to H_2O , HF, Ti, and Mg, which form in *deeper atmospheric layers*. Therefore, these distinct spectral lines allow us to probe the gas dynamics at different atmospheric heights. The VLTI fringe tracker FINITO was not used because it was saturated by the high brightness of R Dor.

We observed Canopus (α Car, spectral type A9II) for the calibration of the interferometric data and also for the spectroscopic calibration. We adopted the angular diameter of 6.93 ± 0.15 mas based on fitting with a linearly limb-darkened disk (Domiciano de Souza et al. 2008). A journal of our observations is given in Table A1.

2.2. Data reduction

The recorded spectrally dispersed interferograms were processed with amdlib ver. 3.0.7², which outputs the squared visibility amplitude, closure phase, and wavelength-differential phase, together with the spatially unresolved flux (i.e., spectrum) as a function of wavelength based on the P2VM algorithm (Tatulli et al. 2007; Chelli et al. 2009). Before processing with amdlib, all the raw data were spectrally binned to a spectral resolution of 8000 with a running box filter to increase S/N sufficiently high for the image reconstruction as described in Ohnaka et al. (2009, 2011, 2013). The interferometric observables (squared visibility amplitude, closure phase, and wavelength-differential phase) of each data set were computed by taking the average of all frames (N_f), discarding 20% of the frames with the lowest fringe S/N.

We used the telluric lines observed in the spectrum of Canopus for the wavelength calibration. The observed spectrum of Canopus was first spline-interpolated, and the pixel positions (i) of the identified telluric lines were fitted with a quadratic function, $\lambda = a + bi + ci^2$. The uncertainty of the wavelength calibration is $7.7 \times 10^{-6} \mu\text{m}$ (1.0 km s^{-1}).

The spectrum of R Dor can be spectroscopically calibrated with that of Canopus as $F_{\text{sci}}^{\text{true}} = F_{\text{sci}}^{\text{obs}} \times F_{\text{cal}}^{\text{true}} / F_{\text{cal}}^{\text{obs}}$, where $F_{\text{sci}(\text{cal})}^{\text{true}}$ and $F_{\text{sci}(\text{cal})}^{\text{obs}}$ denote the true and observed spectra of the science target (R Dor) or the calibrator (Canopus), respectively. A spectroscopically calibrated high-resolution spectrum of Canopus can be used as $F_{\text{cal}}^{\text{true}}$. However, we found none in the literature for the observed wavelength region. Therefore, we used as a proxy of Canopus the high-resolution spectrum of HD6130 obtained by Park et al. (2018), because the spectral type of HD6130, F0II, is close to that of Canopus. The spectrum of HD6130 originally obtained with a spectral resolution of 45 000 was convolved to the spectral resolution of 8 000 of our AMBER data before the spectroscopic calibration of R Dor.

3. ANALYSIS

3.1. Limb-darkened disk fitting

Fitting the observed visibilities with a limb-darkened disk is useful for obtaining an approximate size of the object as a function of wavelength. The best-fit limb-darkened disk model can also be used as the initial model for the image reconstruction. Figure 2 shows the results of fitting with a power-law-type limb-darkened disk (Hestroffer 1997). We estimated the errors in two parameters—limb-darkened disk diameter and limb-darkening parameter—at each wavelength channel using the bootstrap method (Efron & Tibshirani 1993). Then we took the mean of these parameters at the continuum spectral channels (avoiding the H_2O lines that give rise to the increases in the limb-darkened disk diameter) as representative values in the continuum. Because the errors are dominated by the systematic errors in the absolute calibration of the visibilities, the errors were not reduced by a factor of $1/\sqrt{N_{\text{cont}}}$, where N_{cont} is the number of the continuum spectral channels. Instead we took the mean of the errors at the continuum channels. We obtained a limb-darkened disk diameter and a limb-darkening parameter of 51.18 ± 2.24 mas and 0.61 ± 0.24 , respectively, in the continuum. The angular size is in fair agreement with the uniform-disk diameter of 57 ± 5 mas measured at 1.25 μm by Bedding et al. (1997).

In the CO band head at 2.294 μm and individual CO lines, the limb-darkened disk diameter increases up to ~ 80 mas, while the limb-darkening parameter increases

² http://www.jmmc.fr/data_processing_amber.htm

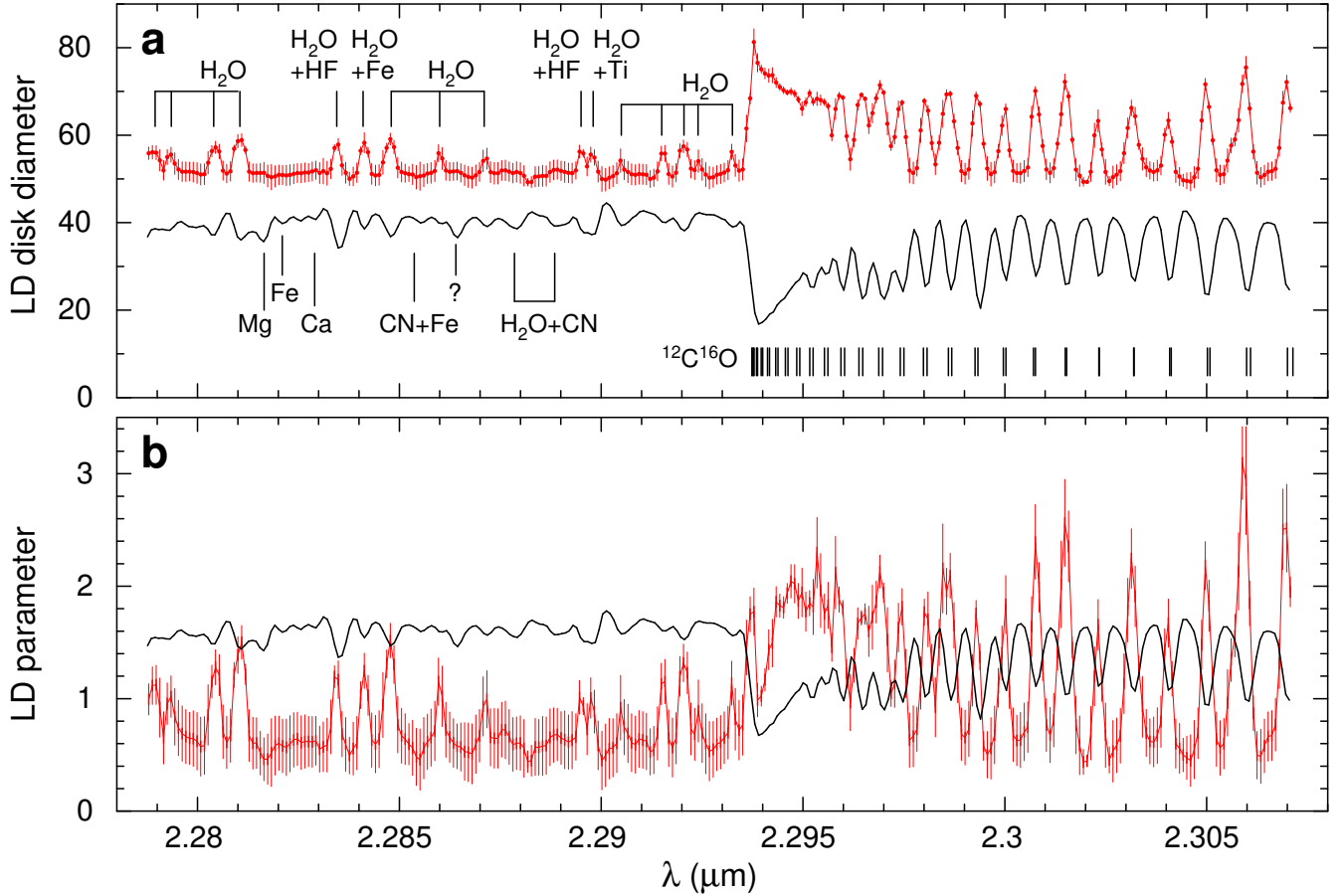


Figure 2. Power-law-type limb-darkened (LD) disk fitting of the AMBER data of R Dor. **a:** Limb-darkened disk diameter (red line) and the scaled observed spectrum (black line). The CO and H₂O lines that give rise to the increases in the limb-darkened disk diameter and the limb-darkening parameter are marked. Other atomic and molecular lines without a increase in the limb-darkened disk diameter are also marked. While the wavelength of the line at 2.2864 μm coincides with a cobalt line, it is possible that it is blended with an unidentified line as discussed in Ohnaka et al. (2019). **b:** Limb-darkening parameter (red line) and the scaled observed spectrum (black line).

up to 2–3. However, the reduced χ^2 of the fitting is 10–30 in the continuum and as large as 70 in the CO lines. This indicates the presence of surface structures in the continuum and more complex structures in the lines, which indeed manifest themselves as the large, bright region over the surface and the extended atmosphere in the reconstructed images as presented in Section 4.

It is worth noting that some spectral lines shortward of the CO band head give rise to spike-like increases in the limb-darkening diameter as well as in the limb-darkening parameter, even though they appear to be weak in the spatially unresolved (i.e., spatially averaged over the stellar disk and the atmosphere) spectrum. As identified in Figure 2, most of these lines are due to H₂O, some of which are blended with other atomic or molecular lines. This was reported in the visibility analysis of the M7 giant SW Vir (Ohnaka et al. 2019) and modeled

by the H₂O layer extending out to $\sim 2 R_*$. The H₂O lines appear to be weak in the spatially unresolved spectrum, because the H₂O absorption expected over the stellar disk is filled in by the emission due to the same H₂O lines originating from the extended H₂O layer. As we present in Section 4.1, the extended H₂O layer manifests itself in the images reconstructed in these H₂O lines.

3.2. Hydrostatic photospheric model

As a reference for the measurement the line-of-sight velocity from spectral lines in spatially resolved spectra presented in Section 4.3, we used a synthetic spectrum computed from the spherical MARCS model atmosphere (Gustafsson et al. 2008) with the parameters appropriate for R Dor. The MARCS model atmospheres are specified by effective temperature, surface gravity, micro-turbulent velocity, chemical composition,

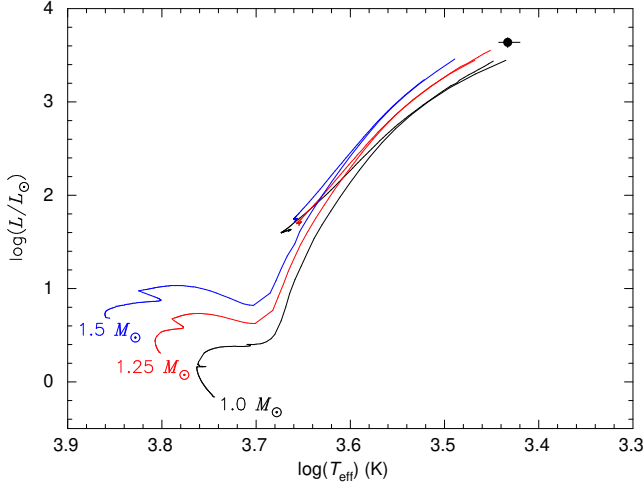


Figure 3. H-R diagram with the position of R Dor (filled circle) and evolutionary tracks with $Z = 0.014$ for 1, 1.25, and $1.5 M_{\odot}$ stars from Lagarde et al. (2012).

Table 1. Basic parameters of R Dor

	Measured	MARCS model
Distance (pc)	55 ± 3^a	—
Bolometric flux (W m^{-2})	4.71×10^{-8}	—
Luminosity (L_{\odot})	4350 ± 520	1326
T_{eff} (K)	2710 ± 70	2700
Radius (R_{\odot})	298 ± 21	165
$\log g$ (cm s^{-2})	-0.6 ± 0.1	0.0
Initial mass (M_{\odot})	1–1.25	—
Current mass M_{\star} (M_{\odot})	0.7–1.0	1
v_{micro} (km s^{-1})	2.0^b	2.0
[Fe/H]	—	0.0
Chemical composition	—	moderate-CN
Age (Gyr)	6–14	—

^aBased on the parallax from van Leeuwen (2007).

^bAdoped from Ryde & Eriksson (2002).

and stellar mass. We determined these parameters as follows.

We first calculated the bolometric flux by collecting the photometric and spectrophotometric data from the visible to the mid-infrared (Mermiliod 1987; Ducati 2002; Stewart et al. 2015; Sloan et al. 2003). A visible extinction A_V of 0.090 was derived from the three-dimensional map of the interstellar extinction presented by Arenou et al. (1992). The collected (spectro)photometric data were then de-reddened by applying the wavelength-dependence of the interstellar

extinction of Cardelli et al. (1989). The bolometric flux was derived to be $4.71 \times 10^{-8} \text{ W m}^{-2}$. We estimated the uncertainty in the bolometric flux to be 5% based on the infrared light curves at 1.25, 2.2, 3.5, and $4.9 \mu\text{m}$ reported by Price et al. (2010). Since the majority of the flux is emitted between 1 and $5 \mu\text{m}$, the variability at shorter or longer wavelengths does not noticeably affect the estimate of the bolometric flux. Combined with the measured limb-darkened disk diameter of $51.18 \pm 2.24 \text{ mas}$, we obtained an effective temperature (T_{eff}) of $2710 \pm 70 \text{ K}$.

The derived luminosity is $4350 \pm 520 L_{\odot}$ based on the bolometric flux and the measured parallax of $18.31 \pm 0.99 \text{ mas}$ (van Leeuwen 2007). Figure 3 shows a comparison of the position of R Dor on the HR-diagram with the theoretical evolutionary tracks of 1, 1.25, and $1.5 M_{\odot}$ stars with the solar metallicity ($Z = 0.014$) from Lagarde et al. (2012). While none of these theoretical evolutionary tracks reaches the luminosity of R Dor, those with the initial stellar masses of 1– $1.25 M_{\odot}$ are the closest to the observed value. This suggests an age of 14 Gyr and 6 Gyr with a current stellar mass of $0.7 M_{\odot}$ and $1.0 M_{\odot}$ for the initial mass of 1 and $1.25 M_{\odot}$, respectively. Therefore, the star has lost $\sim 0.3 M_{\odot}$ in either case. The stellar radius estimated from the measured limb-darkened disk diameter and distance is $298 \pm 21 R_{\odot}$. Then the surface gravity is estimated to be $\log g = -0.6 \pm 0.1$. We adopted a micro-turbulent velocity (v_{micro}) of 2 km s^{-1} as in the previous analysis of the infrared spectrum of R Dor by Ryde & Eriksson (2002).

The MARCS model with the parameters closest to those of R Dor is specified by $T_{\text{eff}} = 2700 \text{ K}$, $\log g = 0.0$, $M_{\star} = 1 M_{\odot}$, and $v_{\text{micro}} = 2 \text{ km s}^{-1}$. We assumed $[\text{Fe}/\text{H}] = 0.0$ and the “moderately CN-cycled” chemical composition of the MARCS model grid, which is appropriate for oxygen-rich AGB stars. The derived basic parameters of R Dor, together with those of the best MARCS model for R Dor, are summarized in Table 1. The luminosity and the stellar radius of the MARCS model are significantly lower and smaller than those observationally derived. This is because the surface gravity of the best MARCS model is still smaller than the observationally estimated value (no MARCS model with $\log g \approx -0.6$ is available for the T_{eff} of R Dor). However, the model spectrum is primarily used to ascertain the wavelengths of the spectral lines for the measurement of the line-of-sight velocity, not the line strengths, which may be affected by the difference in the surface gravity. Therefore, the measurement of the line-of-sight velocity over the reconstructed images presented in Sec-

tion 4.3 is little affected by the difference in the surface gravity.

In the calculation of the synthetic spectrum in the observed wavelength region, we included the lines of $^{12}\text{C}^{16}\text{O}$, $^{12}\text{C}^{17}\text{O}$, $^{12}\text{C}^{18}\text{O}$, $^{13}\text{C}^{16}\text{O}$, $^1\text{H}_2^{16}\text{O}$, $^{12}\text{C}^{14}\text{N}$, $^{13}\text{C}^{14}\text{N}$, and $^1\text{H}^{19}\text{F}$, as well as atomic lines based on the line lists available in the literature (Goorvitch 1994; Polyansky et al. 2018; Sneden et al. 2014; Jorissen et al. 1992; Kurucz & Bell 1995)³. The synthetic spectrum was convolved to the spectral resolution of 8000 of the spectrally binned AMBER data. Then it was shifted in wavelength from the laboratory frame to the observed frame, accounting for the Earth’s motion at the time of the observations and the systemic velocity of R Dor. Since spectral lines in the visible and near-infrared are affected by stellar pulsation and convection (e.g., Hinkle et al. 2002), they are not optimal for deriving the systemic velocity of the star. Instead, radio and far-IR observations of molecular lines originating from approximately spherically expanding circumstellar envelopes are often used to obtain the systemic velocity. The values for R Dor in the literature range from 6 to 8 km s^{−1} in the local standard of rest (González Delgado et al. 2003; Decin et al. 2018; Homan et al. 2018). In the present work, we adopted the 7.5 km s^{−1} recently derived by Van de Sande et al. (2018) and Homan et al. (2018), which translates into a heliocentric velocity of 23.9 km s^{−1}.

3.3. Image reconstruction

We reconstructed the image at each wavelength channel using MiRA ver 0.9.9⁴ (Thiébaud 2008). We applied the technique to restore the Fourier phases from wavelength-differential phase measurements (Petrov et al. 2007; Schmitt et al. 2009; Millour et al. 2011; Ohnaka et al. 2011, 2013; Weigelt et al. 2016; Ohnaka et al. 2017b). The restored Fourier phases were used for the image reconstruction together with the squared visibility amplitudes and closure phases. We also carried out reconstruction experiments with simulated data to examine the reliability of the image reconstruction from the observed data. Details of the image reconstruction are described in Appendix B.

The reconstructed images were convolved with a two-dimensional Gaussian beam with a full width at half

maximum (FWHM) of $\lambda/B_{\text{max}} = 6.8$ mas, where λ was taken to be the central wavelength of the observed spectral window (2.3 μm), and B_{max} is the maximum projected baseline length of our observations (70 m). As presented in Appendix B, we carried out the image reconstruction both with the quadratic (Tikhonov) regularization and the maximum entropy regularization with different reconstruction parameters. We computed the median from the images reconstructed with different reconstruction parameters at each wavelength channel.

4. RESULTS

4.1. Wavelength-dependent images of the surface and extended atmosphere

Figure 4 shows images of R Dor reconstructed at nine representative wavelength channels in different spectral lines as well as in the continuum. The image reconstructed in the continuum (Figure 4e) shows a large, irregularly shaped bright region over the stellar surface, which is well resolved with the angular resolution of 6.8 mas—seven times finer than the star’s angular diameter of 51.2 mas. The intensity contrast of the bright region with respect to the surrounding region is about 25%. This is very different from the surface of the red supergiant Antares seen in the continuum, which only exhibits a weak, large spot with an intensity contrast of 3–4% (Ohnaka et al. 2017b). The presence of a high-contrast bright region is qualitatively consistent with the latest three-dimensional convection simulations of AGB stars (Freytag et al. 2017). As will be discussed in Section 5, dust formation is detected at $\sim 1.5 R_*$ toward R Dor (Norris et al. 2012; Khouri et al. 2016). However, the contribution of dust in the observed continuum images is likely to be negligible, because the flux contribution of dust-scattered light is estimated to be only $\sim 1.4\%$ at 2.06 μm for R Dor (Norris et al. 2012).

The image reconstructed in the Mg line (Figure 4a) appears to be nearly the same as the continuum image without a noticeable trace of an extended atmosphere. This suggests that the Mg line originates in deep layers (i.e., close to the star), whose geometrical thickness is not spatially resolved with the resolution of 6.8 mas. Therefore, the line probes atmospheric heights lower than $\sim 1.13 R_*$ (measured from the stellar center). However, the images reconstructed in the H₂O lines shown in Figures 4b and 4c (the former line blended with an HF line) show an extended atmosphere with a radius of ~ 38 mas ($\sim 1.5 R_*$). Moreover, the CO line images (Figures 4f–4i) show an atmosphere even more extended out to $\sim 1.8 R_*$. The intensity contrast of the bright region over the surface increases from the 25% in the continuum to $\sim 40\%$ in the H₂O and CO line images. It may

³ H₂O: <http://www.exomol.com/data/molecules/H2O/1H2-16O/POKAZATEL/>

CN: <https://www.as.utexas.edu/~chris/lab.html>

Atomic lines: <https://www.cfa.harvard.edu/amp/ampdata/kurucz23/sekur.html>

⁴ <http://cral.univ-lyon1.fr/labo/perso/eric.thiebaud/?Software/MiRA>

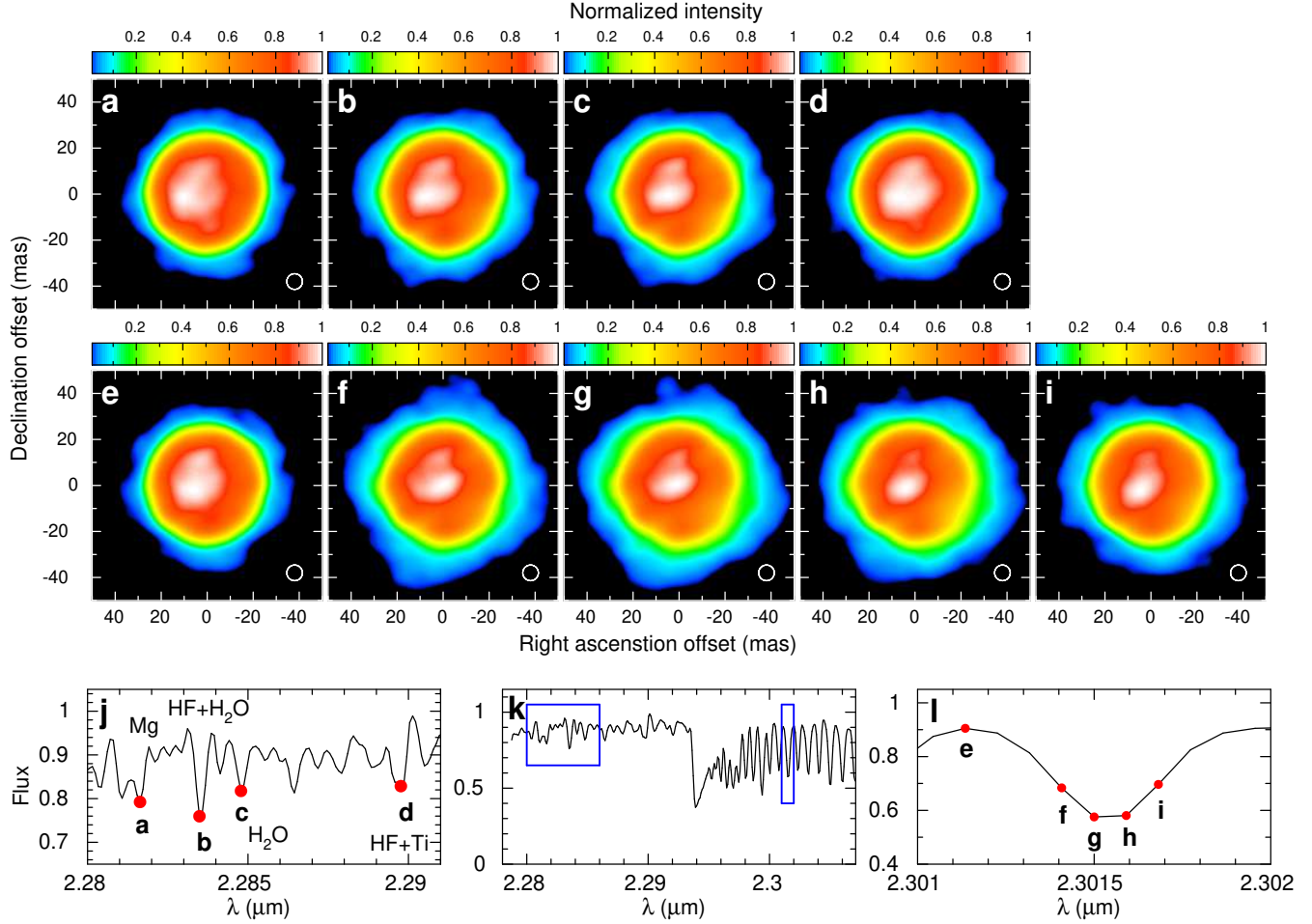


Figure 4. Wavelength-dependent images of the surface and extended atmosphere of R Dor. The images reconstructed at nine representative wavelength channels in the molecular and atomic lines of Mg, Ti, HF, and H₂O (panels a–d) and across one of the CO lines (panels e–i) are shown. Each image is normalized with the maximum intensity. The color scale is set so that the intensity lower than 1% of the maximum intensity is cut off (appearing in black), to show the images used for the derivation of the line-of-sight velocity maps as described Section 4.3. The image in the continuum (e) shows a large, bright region over the stellar disk, which can also be seen in the images in the molecular and atomic lines. It should be noted, however, that the intensity contrast differs in the continuum ($\sim 25\%$) and in the lines ($\sim 40\%$). The extended atmosphere outside the stellar disk can be seen in the images obtained in the H₂O lines (b and c), and appears more pronounced in the images obtained in the CO line (f, g, and h). The beam size (6.8×6.8 mas) is shown in the lower right corner of each panel. North is up, east to the left. Panels j–l: Spectrum of R Dor in the entire spectral range of our observations is shown in k. Enlarged views of two wavelength ranges (marked with the rectangles in panel k) are shown in panels j and l, where the wavelength channels of the images in panels a–i are marked with the corresponding alphabetic characters.

represent a region with higher temperatures throughout the atmosphere.

We note that the hydrostatic MARCS photospheric model with the parameters appropriate for R Dor extends only to $1.12 R_\star$. As mentioned in Section 3.2, the surface gravity of the best MARCS model ($\log g = 0.0$) is still smaller than the observationally estimated value ($\log g = -0.6$). Since the geometrical thickness of the atmosphere with respect to the stellar radius, $\Delta r/R_\star$, is proportional to $g^{-1/2}$ (Jørgensen et al. 1992), the geometrical thickness of the MARCS photospheric model

after correcting for the difference in the surface gravity is 0.24. This means that the photosphere extends only to $1.24 R_\star$ at most. Therefore, the extended outer atmosphere seen in the H₂O and CO line images cannot be explained by the hydrostatic model atmosphere. Such extended atmospheres in Mira-type AGB stars are fairly explained by large-amplitude stellar pulsation (e.g., Wittkowski et al. 2008, 2011; Hillen et al. 2012). However, R Dor is a semiregular variable, and its variability amplitude is $\Delta V \approx 1.5$ mag based on the light curve compiled by the American Association of Vari-

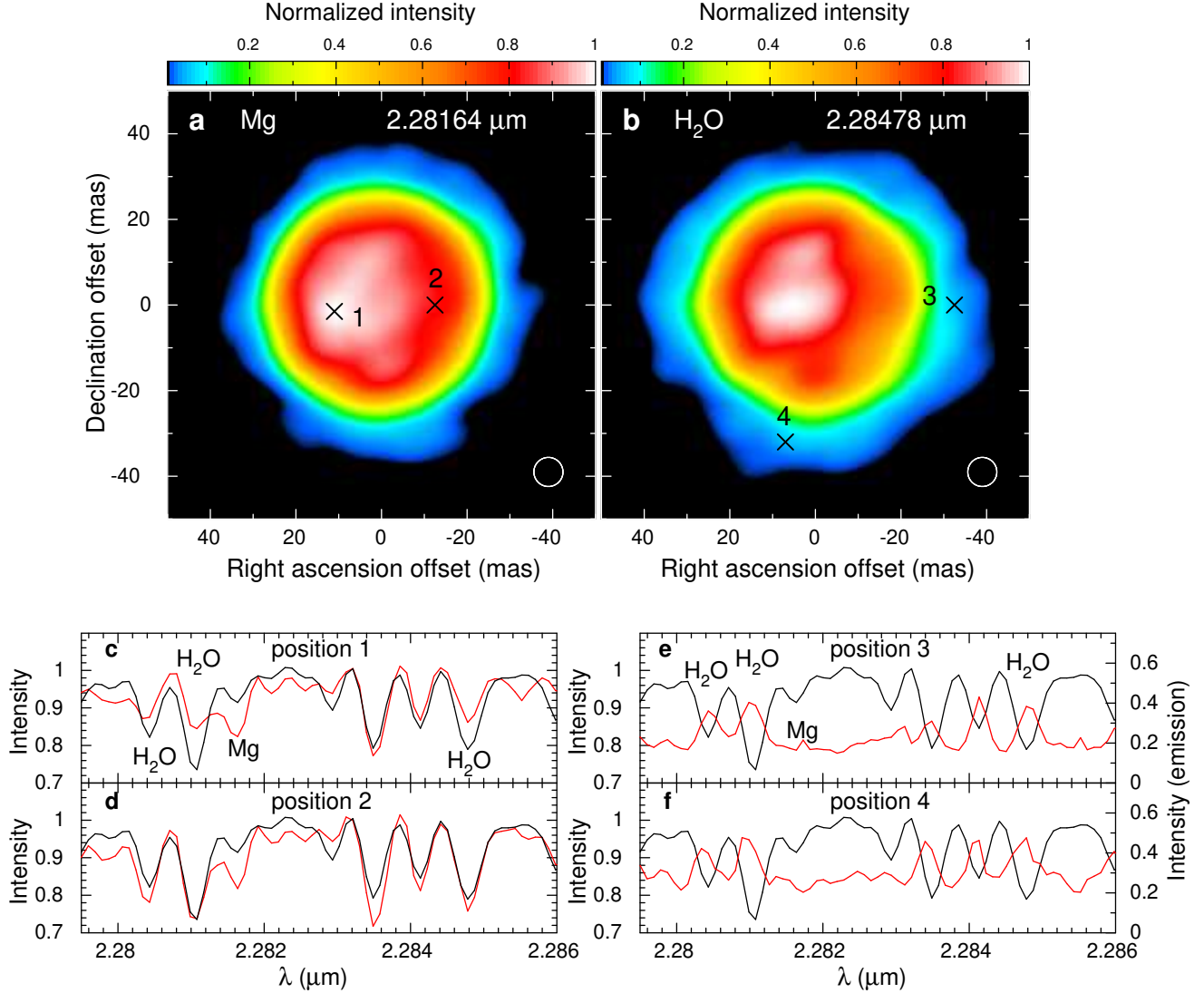


Figure 5. Spatially resolved spectra of the lines of Mg and H₂O obtained over the surface and atmosphere of R Dor. The Mg and H₂O lines probe the gas dynamics at atmospheric heights of $\lesssim 1.13 R_*$ and $\sim 1.5 R_*$, respectively. **a** and **b**: The images reconstructed at the center of the Mg line at $2.28164 \mu\text{m}$ and the H₂O line at $2.28478 \mu\text{m}$, respectively. The positions 1, 2, 3, and 4 are where the spatially resolved spectra exemplarily shown in **c–f** were extracted. North is up, east is to the left. **c–f**: Spatially resolved spectra obtained at the positions 1, 2, 3, and 4 are shown by the red lines. The emission line spectra at positions 3 and 4 are scaled, as shown in the right abscissa, to facilitate the visual inspection. The black lines show the synthetic spectrum computed from the spherical hydrostatic photospheric model without atmospheric motion. The Mg and H₂O lines used to derive the maps of the line-of-sight velocity (Figures 7a and 7b) are identified. The spatially resolved spectra of these lines obtained at the positions 1, 2, and 3 (panels **c**, **d**, and **e**) do not show clear wavelength shifts with respect to the hydrostatic model spectrum, in contrast to the CO line spectra shown in Figure 6. Only in the spectrum at the position 4 (panel **f**) do the H₂O lines show some blueshifts.

able Star Observers (AAVSO). This is much smaller than that of typical Mira-type AGB stars. The presence of the extended atmosphere has been detected in other non-Mira type AGB stars by infrared-interferometric observations in the CO and H₂O lines but without images so far (e.g., Martí-Vidal et al. 2011; Ohnaka et al. 2012, 2019). Our H₂O and CO line images of R Dor are the

first images of the extended atmosphere of a non-Mira AGB star.

4.2. Spatially resolved spectra over the surface and extended atmosphere

The images reconstructed at 309 wavelength channels across the CO lines and other spectral lines allowed us to extract the spatially resolved spectrum at each posi-

tion over the surface and atmosphere of the star. For this purpose, the intensity of the image reconstructed and convolved with the beam at each wavelength channel was scaled so that the flux integrated over the entire image is equal to the flux observed in the spectroscopically calibrated spectrum of R Dor.

Figure 5 shows the spatially resolved spectra across the lines of Mg and H₂O (red lines) obtained at four different positions marked in Figures 5a and 5b. Also shown is the synthetic spectrum (black lines) computed from the hydrostatic MARCS photospheric model (without atmospheric motion) with the parameters appropriate for R Dor as described in Section 3.2. At the positions over the stellar surface, the lines in the spatially resolved spectrum appear in absorption (Figures 5c and 5d). However, the H₂O lines at the positions 3 and 4 over the atmosphere turn into emission (Figures 5e and 5f), as expected from Kirchhoff's law. The Mg line at 2.28164 μm does not appear in emission at the positions 3 and 4, because as seen in Figures 4a and 4e the extension of the Mg line image is nearly the same as the continuum image. It is worth noting, compared to the CO lines described below, that the Mg and H₂O lines appear approximately at the wavelengths predicted by the hydrostatic model without significant wavelength shifts, except for the position 4 where the H₂O emission lines show some blueshifts (Figure 4f).

Figures 6 shows the spatially resolved spectra of the CO lines (red lines) at three positions, together with the synthetic spectrum predicted by the hydrostatic MARCS photospheric model (black lines). Figures 6b–6d show the results for the entire observed spectral window. As in the case of the H₂O lines described above, the CO lines appear in prominent emission at the positions 2 and 3 over the atmosphere. The other spectral lines shortward of the CO band head at 2.2935 μm , mostly H₂O lines, also appear in emission at position 2 as already discussed above. The H₂O emission lines are not present in the spatially resolved spectrum at the position 3, because it is outside the extended H₂O atmosphere seen in Figures 4b and 4c.

Figures 6e–6g show an enlarged view of the spatially resolved spectra across four CO lines. For the position 1 over the surface, the ratioed spectrum (i.e., the spatially resolved spectrum divided by the model spectrum) is also presented (blue line in Figure 6e) to facilitate to see the wavelength shifts of the CO lines. Unlike the case of the Mg and H₂O lines, the spatially resolved spectra (as well as the ratioed spectrum) reveal that the CO lines are blueshifted with respect to the hydrostatic model spectrum. The images across the CO line shown in Figure 4 reveal that the blue-wing image (Figure 4f)

appears more extended than the red-wing image (Figure 4i), although the flux is nearly the same (Figure 4l). This asymmetric appearance of the image across the CO line profiles leads to the blueshifts in the spatially resolved spectra. The blueshifts of the CO lines detected over the surface and extended atmosphere suggest that the gas is moving toward us.

4.3. Velocity-field maps over the surface and extended atmosphere

The line-of-sight velocity at each position over the surface and atmosphere of the star was computed by taking the cross-correlation between the spatially resolved spectrum and the synthetic spectrum from the hydrostatic MARCS model (shifted to the observed wavelength frame as described above). To obtain a velocity-field map from the CO lines, the cross-correlation was computed for the lines between 2.3 and 2.308 μm , where the individual lines are resolved. For the velocity-field maps from other atomic and molecular lines, we selected the Mg line at 2.28164 μm and three H₂O lines at 2.28043, 2.28099, and 2.28478 μm , because they are mostly free of blends due to other spectral lines. The three H₂O lines have similar gf -values and lower excitation potentials, which means that they form approximately at the same atmospheric height. Therefore, we took the median of the velocity-field maps derived from three H₂O lines to obtain a more reliable result. Other H₂O lines responsible for the increases in the limb-darkened disk diameter and limb-darkening parameter (Figure 2) were not used, because their line profiles are affected by the adjacent lines. Other atomic and molecular lines present in the observed spectral window are affected by the blend and could not be used to extract velocity-field maps. We measured the line-of-sight velocity at the positions where the intensity is higher than 1% of the maximum intensity of the images at the line center to avoid unreliable velocity measurements at very low intensities.

Figure 7 shows the maps of the line-of-sight velocity derived from the Mg, H₂O, and CO lines, together with the 1σ uncertainty in the velocity measurement (see Appendix B for the estimate of the uncertainty). As expected from the spatially resolved spectra, the line-of-sight velocity maps of the Mg and H₂O lines, shown in Figures 7a and 7b, show that the atmospheric layers in which these lines form ($\lesssim 1.13 R_\star$ and $\sim 1.5 R_\star$ for the Mg and H₂O lines, respectively) are mostly quiet without significant systematic or turbulent motion greater than the measurement uncertainty of $\pm 1.7 \text{ km s}^{-1}$ (Figures 7d and 7e, see also Appendix B). Only in the southern and northwestern regions of the H₂O atmo-

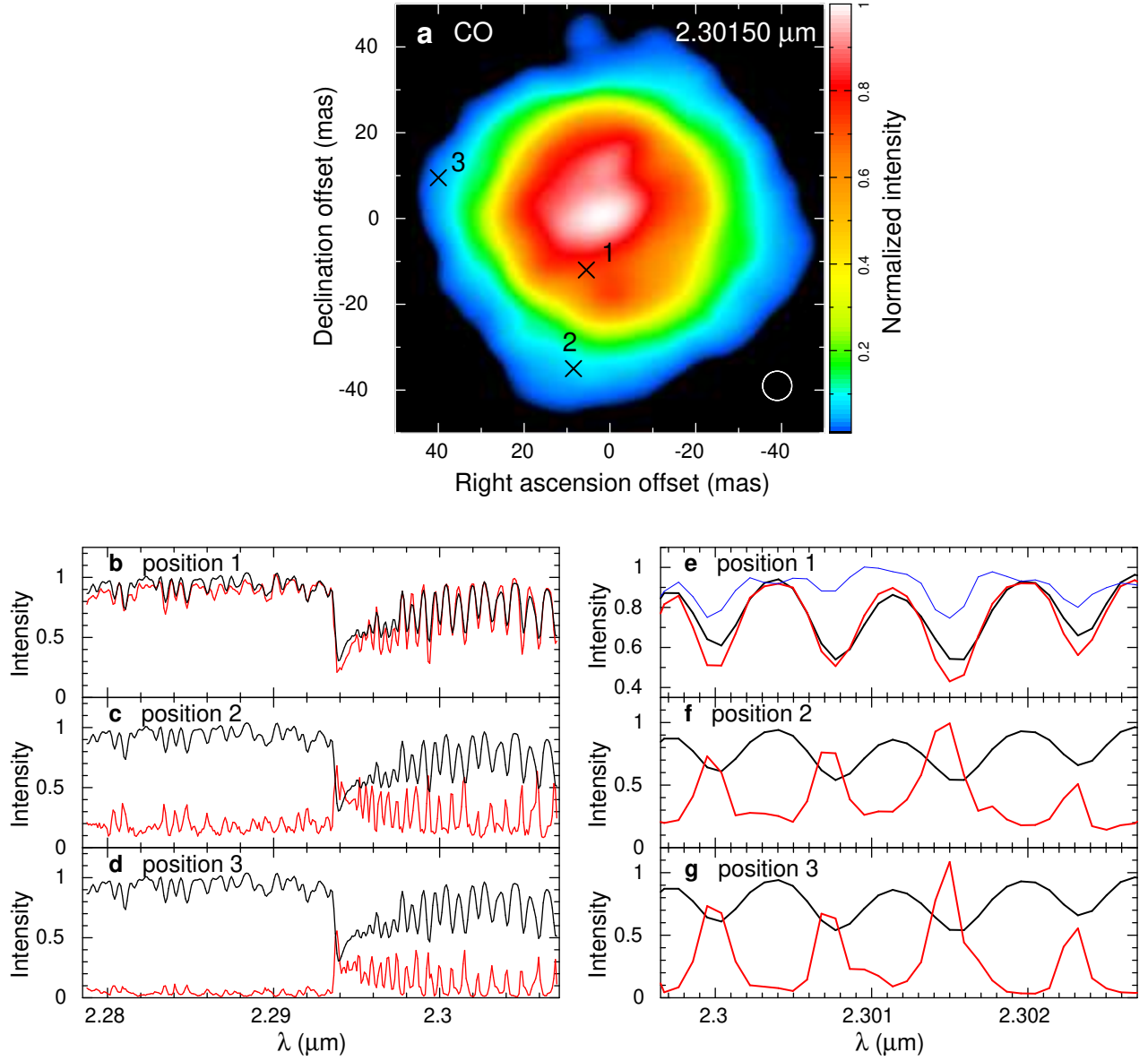


Figure 6. Spatially resolved CO line spectra obtained over the surface and atmosphere of R Dor. **a:** The image reconstructed at the center of the CO line at $2.30150 \mu\text{m}$. The positions 1, 2, and 3 are where the spatially resolved spectra exemplarily shown in panels **b–g** were derived. North is up, east is to the left. Panels **b–d:** Spatially resolved spectra obtained at the positions 1, 2, and 3 in the entire observed spectral range are shown by the red lines. The spectra at the positions 2 and 3 are scaled to facilitate the visual inspection. The synthetic spectrum computed from the hydrostatic photospheric model is shown by the black lines. The spatially resolved spectra extracted off the limb of the star (panel **c**) show not only the CO emission lines but also other spectral lines shortward of the CO band head, mostly due to H_2O , clearly in emission. Panels **e–g:** Spatially resolved spectra obtained at the positions 1, 2, and 3 across four CO lines are shown by the red lines. The synthetic spectrum computed from the hydrostatic photospheric model is shown by the black lines. In panel **e**, the ratioed spectrum obtained by dividing the spatially resolved spectrum by the hydrostatic model spectrum is also plotted by the blue line to show more clearly the blueshift of the CO lines with respect to the model spectrum. The ratioed spectrum at the position 1 as well as the CO emission lines extracted at the positions 2 and 3 are blueshifted, suggesting that the gas is moving toward us.

sphere do we detect noticeable line-of-sight velocities of about -8 km s^{-1} . The northern region also shows large positive and negative line-of-sight velocities of up to $\pm 10 \text{ km s}^{-1}$. However, the uncertainty in the measurement is larger, $\sim 5 \text{ km s}^{-1}$, as shown in Figure 7e. Therefore, while there is some gas motion in this region, its amplitude may be less significant, smaller than $\pm 10 \text{ km s}^{-1}$.

In marked contrast, the line-of-sight velocity map obtained from the CO lines, shown in Figure 7c, reveals outward motion at velocities of $7\text{--}15 \text{ km s}^{-1}$ over a significant fraction of the surface and atmosphere extending out to $\sim 1.8 R_*$. The strongest outward motion at up to 15 km s^{-1} is found in the southern region of the extended atmosphere. The southern half of the stellar disk adjacent to this region also shows outward motion. The velocity-field map derived from the H_2O lines also shows outward motion at $\sim 8 \text{ km s}^{-1}$ in this region as mentioned above. The regions in the northeast and the west of the CO atmosphere also show outward motion at $7\text{--}10 \text{ km s}^{-1}$. There are two small regions with positive line-of-sight velocities (i.e., moving away from us) in the north and in the south. However, as Figure 7f shows, the uncertainty in the velocity is large at these positions, $5\text{--}10 \text{ km s}^{-1}$. Therefore, we cannot conclude the presence of downdrafting motion in these regions. Comparison of the velocity-field maps obtained from the Mg, H_2O and CO lines suggests strong acceleration of material between ~ 1.5 and $1.8 R_*$. This is the first three-dimensional diagnosis of the atmospheric dynamics from the low (i.e., deep) photospheric layers to the extended outer atmosphere for a star other than the Sun.

The CO lines are estimated to be optically thick, if we adopt the CO column density and temperature estimated for M giants with stellar parameters similar to R Dor (Ohnaka et al. 2012, 2019). If we assume a spherically symmetric atmosphere as modeled in these previous works, the CO lines remain optically thick to the extreme limb of the CO atmosphere. If the outward gas motion is spherically symmetric, the line-of-sight velocity is expected to fall off to zero toward the edge of the extended atmosphere. However, it is difficult to measure the line-of-sight velocity just at the extreme limb of the atmosphere owing to the finite spatial resolution. Moreover, the line-of-sight velocity cannot be measured out to the real edge of the extended atmosphere, because the intensity is too low to reliably measure the line-of-sight velocity as mentioned above. In fact, as Figures 7e and 7f show, the uncertainty in the velocity measurement is high at the edge of the H_2O and CO atmosphere.

Despite the blueshift over a large fraction of the surface and atmosphere, the spatially unresolved spectrum

does not show a noticeable blueshift for the following reason. The CO lines originate not only from the extended atmosphere but also from the lower, static photosphere. The contribution from the outwardly moving extended atmosphere leads to blueshifted absorption over the stellar disk. However, the blueshifted emission from the extended atmosphere seen outside the star's limb fills in the blueshifted absorption. Therefore, when averaged over the surface and atmosphere, the spectrum does not show a noticeable blueshift.

The gas motion detected in R Dor is very different from the dynamics of the extended atmosphere of the red supergiant Antares, which is characterized by turbulent motion of large gas clumps without any systematic outward or inward motion (Ohnaka et al. 2017b). The line-of-sight velocities of $7\text{--}15 \text{ km s}^{-1}$ seen in the extended atmosphere are higher than the terminal velocity of $\sim 5.5 \text{ km s}^{-1}$ that the stellar wind is supposed to reach at distances greater than $\sim 20 R_*$ (Van de Sande et al. 2018). Decin et al. (2018) detected velocity components much faster than the terminal velocity in some submillimeter molecular lines toward R Dor, indicating a strong wind acceleration in addition to the slower wind. The outward motion seen in the line-of-sight velocity map of the CO lines may give rise to the high-velocity components detected in the submillimeter lines.

The velocity-field maps obtained from the H_2O and CO lines (Figures 7b and 7c) show ring-shaped gaps along the limb of the star for the following reason. The spatially resolved spectra across the H_2O and CO lines along the stellar limb show neither absorption nor emission because the absorption and emission cancel out within the finite beam size. Therefore, the velocity could not be measured along the limb of the star, which appears as the black ring-shaped gaps. We also note that as Figures 4a and 4e show, the extension of the image in the Mg line at $2.28164 \mu\text{m}$ is approximately the same as that of the continuum image. Therefore, the spatially resolved spectra do not show the Mg line in emission outside the limb of the star. This is why we could measure the line-of-sight velocity from the Mg line only inside the limb of the star as shown in Figure 7a.

5. DISCUSSION AND CONCLUSION

The formation of clumpy dust clouds has recently been detected toward R Dor, as close as at $\sim 1.5 R_*$, by polarimetric observations of light scattered by dust grains (Norris et al. 2012; Khouri et al. 2016). Therefore, dust already forms approximately at the radius of the atmosphere seen in the H_2O line images. Norris et al. (2012)

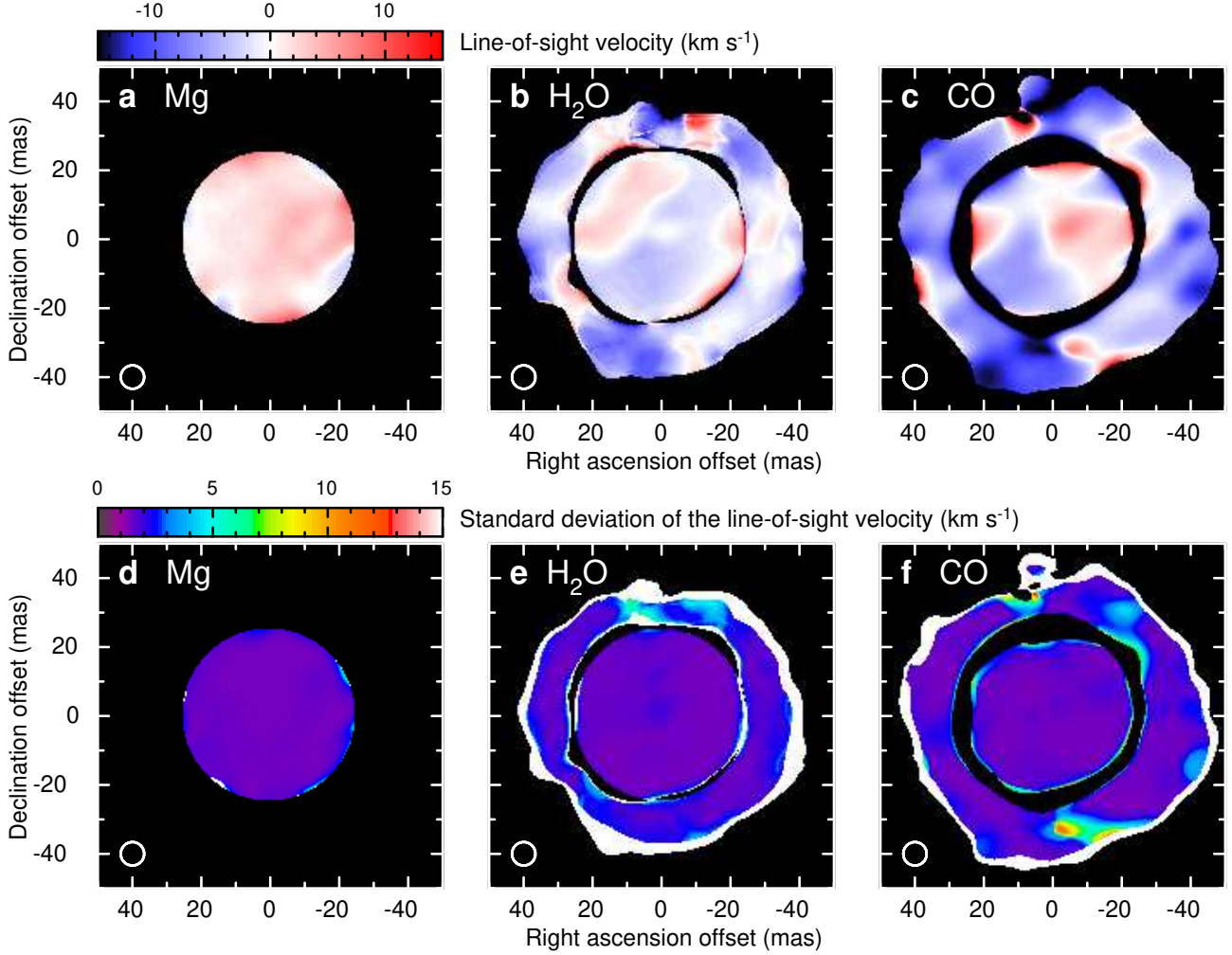


Figure 7. Velocity-field maps obtained at different atmospheric heights of R Dor. North is up, east is to the left. **a:** Velocity-field map in the deep (low) layers at atmospheric heights lower than $\lesssim 1.13 R_{\star}$ (measured from the stellar center) obtained from the Mg line at $2.28164 \mu\text{m}$. **b:** Velocity-field map at an atmospheric height of $\sim 1.5 R_{\star}$ obtained by averaging the velocity-field maps computed from three H_2O lines at 2.28043 , 2.28099 , and $2.28478 \mu\text{m}$. **c:** Velocity-field map at an atmospheric height of $\sim 1.8 R_{\star}$ obtained from the CO first overtone lines. **d–f:** Standard deviation (1σ) of the line-of-sight velocity derived from the Mg, H_2O , and CO lines. The uncertainty in the velocity is at most $\sim 1.7 \text{ km s}^{-1}$ in most regions over the surface and atmosphere (see Appendix B for details). The black, ring-shaped gaps in the velocity-field maps of the H_2O and CO lines correspond to the limb of the star. The spatially resolved spectra on the limb show neither absorption nor emission because the absorption and emission cancel out within the finite beam size shown in the lower left corner. Therefore, the velocity could not be measured.

and Khouri et al. (2016) propose Al_2O_3 or Fe-free silicates such as Mg_2SiO_4 and MgSiO_3 as grain species responsible for the scattered light, although their observations did not allow them to nail down the grain species.

The recent three-dimensional convection simulations with dust formation presented by Höfner & Freytag (2019), although the models are more luminous and cooler than R Dor, show that while Al_2O_3 grains form at $\sim 1.4 R_{\star}$, Mg_2SiO_4 mantle forms onto the Al_2O_3 cores farther away, at $1.7\text{--}1.8 R_{\star}$ (Höfner & Freytag 2019). Also, Höfner et al. (2016) suggest that the ra-

diation pressure due to scattering by Al_2O_3 grains is insufficient, and the composite grains with an Al_2O_3 core and Fe-free silicate mantle may drive the stellar wind. The formation radius of Al_2O_3 grains corresponds to the radius of the atmosphere probed with the H_2O lines without significant systematic motion, while the Al_2O_3 +Fe-free silicate grains form approximately at the radius of the atmosphere seen in the CO line images with the systematic outward motion. Therefore, the outward motion detected by our AMBER observations may be caused by the initial acceleration of the stellar

wind driven by the radiation pressure due to scattering by the composite grains.

Tantalizing as the evidence is, it is also possible that the outward motion is simply part of the ballistic atmospheric motion caused by stellar pulsation or convection, not necessarily leading to further acceleration of material. The three-dimensional convection simulations show the ballistic gas motion at $\sim 2 R_*$ (Freytag et al. 2017). However, while dust formation is taken into account in these models, the dynamical effects triggered by the radiation pressure on dust grains are not yet included because it would be computationally very exhaustive. It is not clear either whether or not the outward motion is always present. The submillimeter imaging of R Dor with a resolution of 30×42 mas reported by Vlemmings et al. (2018) using the Atacama Large Millimeter/submillimeter Array (ALMA) shows rotation at a velocity of 1.0 km s^{-1} but no signature of outward motion within 100 mas ($= 4 R_*$), which may indicate time variation in the dynamics in the outer atmosphere.

Interferometric imaging monitoring, together with high angular resolution thermal-infrared imaging of the dust formation region, is a next step to draw a definitive conclusion about whether or not the material is driven outward by the radiation pressure on dust grains, and if so, which grain species is responsible for the acceleration of the stellar wind.

We thank the ESO VLTI team for their support for our VLTI/AMBER observations. K.O. acknowledges the support of the Comisión Nacional de Investigación Científica y Tecnológica (CONICYT) through the FONDECYT Regular grant 1180066. This research made use of the SIMBAD database, operated at the CDS, Strasbourg, France, and NSO/Kitt Peak FTS data on the Earth’s telluric features produced by NSF/NOAO. We acknowledge with thanks the variable star observations from the AAVSO International Database contributed by observers worldwide and used in this research.

Facilities: VLTI(AMBER), AAVSO

Software: amdlib (Tatulli et al. 2007; Chelli et al. 2009), MiRA (Thiébaud 2008)

APPENDIX

A. SUMMARY OF AMBER OBSERVATIONS

The journal of our AMBER observations of R Dor is given in Table A1.

Table A1. Summary of VLTI/AMBER observations of R Dor. B_p : Projected baseline length. PA: Position angle of the baseline vector projected onto the sky. s : Seeing in the visible. τ_0 : Coherence time in the visible. DIT: Detector Integration Time. N_f : Number of frames in each exposure. N_{exp} : Number of exposures.

#	t_{obs} (UTC)	B_p (m)	PA ($^\circ$)	s ($''$)	τ_0 (ms)	DIT $\times N_f \times N_{\text{exp}}$ (ms)
2013 Dec 01 (UTC) D0-G1-H0						
1	02:18:39	63.95/57.20/55.39	46/172/102	1.2	1.6	$120 \times 500 \times 5$
2	03:00:29	63.96/57.56/58.92	55/177/111	0.9	2.0	$120 \times 500 \times 5$
3	03:43:25	63.63/57.56/61.95	64/−177/119	1.1	1.7	$120 \times 500 \times 5$
4	04:27:05	62.85/57.17/64.47	74/−171/127	1.1	1.7	$120 \times 500 \times 5$
5	05:18:07	61.42/56.28/66.59	84/−165/136	1.0	1.8	$120 \times 200 \times 4$
6	05:52:58	59.83/55.21/67.81	92/−160/143	1.2	1.6	$120 \times 500 \times 5$
7	06:33:52	57.74/53.70/68.78	102/−155/151	0.9	2.1	$120 \times 500 \times 5$
8	07:15:54	55.28/51.74/69.47	112/−149/159	1.0	1.9	$120 \times 500 \times 5$
9	07:56:42	52.71/49.42/69.84	122/−144/167	1.3	1.5	$120 \times 500 \times 5$
10	08:40:21	50.04/46.46/70.06	134/−139/176	1.2	1.6	$120 \times 500 \times 5$
2013 Dec 02 (UTC) G1-H0-I1						
11	01:40:43	44.45/28.01/56.63	16/−64/−13	1.6	1.7	$120 \times 500 \times 5$
12	02:20:04	44.05/30.01/57.26	23/−57/ −8	1.2	2.3	$120 \times 500 \times 5$
13	03:00:38	43.44/31.79/57.57	31/−51/ −2	1.4	1.8	$120 \times 500 \times 5$
14	03:40:32	42.61/33.27/57.54	38/−44/ 3	1.1	2.1	$120 \times 500 \times 5$
15	04:19:57	41.53/34.47/57.20	45/−38/ 8	1.3	1.9	$120 \times 500 \times 5$
16	05:00:10	40.15/35.44/56.51	52/−31/ 14	1.0	2.3	$120 \times 500 \times 5$
17	05:41:10	38.40/36.20/55.45	60/−24/ 19	1.0	2.5	$120 \times 500 \times 5$
18	06:21:59	36.32/36.75/54.02	67/−18/ 24	1.1	2.2	$120 \times 500 \times 5$
19	07:01:50	33.96/37.09/52.24	75/−11/ 30	1.1	2.3	$120 \times 500 \times 5$
20	07:42:08	31.27/37.27/50.05	83/ −4/ 35	1.4	1.7	$120 \times 500 \times 5$
2013 Dec 06 (UTC) A0-B2-D0						
21	00:21:54	8.47/30.23/34.89	58/ −5/ 7	1.4	2.7	$120 \times 500 \times 5$
22	00:58:54	8.95/30.27/34.78	68/ 1/ 14	0.9	4.5	$120 \times 500 \times 5$
23	01:32:49	9.39/30.21/34.59	76/ 6/ 21	1.0	3.7	$120 \times 500 \times 5$
24	02:06:43	9.80/30.04/34.32	84/ 12/ 27	1.4	3.0	$120 \times 500 \times 5$
25	02:39:52	10.16/29.78/33.95	91/ 17/ 34	1.1	3.5	$120 \times 500 \times 5$
26	03:12:53	10.47/29.40/33.47	98/ 22/ 40	1.3	2.9	$120 \times 500 \times 5$
27	03:47:02	10.74/28.89/32.82	106/ 28/ 46	1.6	2.2	$120 \times 500 \times 5$
2013 Dec 06 (UTC) A1-B2-C1						
28	05:14:33	11.17/ 8.98/15.16	124/ 41/ 88	2.0	1.9	$120 \times 500 \times 5$
29	05:49:44	11.25/ 8.62/14.75	132/ 47/ 96	2.3	1.7	$120 \times 500 \times 5$
30	06:23:47	11.29/ 8.22/14.30	139/ 52/104	2.2	1.6	$120 \times 500 \times 5$
31	06:57:18	11.31/ 7.78/13.80	146/ 57/112	2.5	1.5	$120 \times 500 \times 5$
32	08:00:50	11.30/ 6.79/12.80	160/ 67/128	2.5	1.5	$120 \times 500 \times 5$

Table A1. (Continued)

#	t_{obs} (UTC)	B_p (m)	PA ($^\circ$)	s ($''$)	τ_0 (ms)	DIT $\times N_f \times N_{\text{exp}}$ (ms)
2013 Dec 07 (UTC) A1-B2-C1						
33	00:01:39	8.26/10.05/15.79	53/ -8/ 19	1.5	2.1	$120 \times 500 \times 5$
34	00:35:04	8.69/10.08/15.85	62/ -3/ 27	1.2	2.5	$120 \times 500 \times 5$
35	01:08:01	9.12/10.08/15.92	71/ 3/ 35	1.6	2.0	$120 \times 500 \times 5$
36	01:46:51	9.61/10.04/15.97	80/ 9/ 44	1.6	1.9	$120 \times 500 \times 5$
37	02:19:58	9.99/ 9.96/15.99	88/ 14/ 51	1.4	2.3	$120 \times 500 \times 5$
38	02:53:02	10.32/ 9.86/15.97	95/ 20/ 58	1.1	3.0	$120 \times 500 \times 5$
39	03:27:31	10.62/ 9.71/15.88	102/ 25/ 66	1.0	3.1	$120 \times 500 \times 5$
40	04:03:34	10.87/ 9.50/15.71	110/ 31/ 74	0.9	3.4	$120 \times 500 \times 5$
41	04:53:03	11.11/ 9.14/15.34	120/ 38/ 84	0.8	3.9	$240 \times 250 \times 5$
42	05:25:56	11.21/ 8.83/14.99	127/ 43/ 92	0.8	3.9	$120 \times 500 \times 5$
43	05:58:47	11.27/ 8.48/14.59	134/ 49/ 99	0.9	3.2	$120 \times 500 \times 5$
44	06:32:43	11.30/ 8.06/14.11	142/ 54/107	0.9	3.4	$120 \times 500 \times 5$
45	07:06:48	11.31/ 7.59/13.59	149/ 59/115	1.1	2.7	$120 \times 500 \times 5$
46	07:39:39	11.30/ 7.08/13.07	157/ 64/124	1.3	2.2	$120 \times 500 \times 5$
47	08:12:35	11.29/ 6.52/12.57	164/ 69/133	1.4	2.1	$120 \times 500 \times 5$
2013 Dec 08 (UTC) B2-C1-D0						
48	00:16:30	10.07/20.17/30.23	-5/ -5/ -5	1.0	2.9	$121 \times 500 \times 5$
49	00:50:22	10.08/20.20/30.27	0/ 1/ 1	0.8	3.4	$121 \times 500 \times 5$
50	01:24:41	10.06/20.15/30.22	6/ 6/ 6	0.8	3.7	$121 \times 500 \times 5$
51	01:57:41	10.01/20.05/30.05	11/ 11/ 11	—	—	$121 \times 500 \times 5$
52	02:31:08	9.92/19.87/29.79	17/ 17/ 17	0.6	4.4	$121 \times 500 \times 5$
53	03:07:35	9.78/19.59/29.37	23/ 23/ 23	0.6	4.3	$121 \times 500 \times 5$
54	03:41:11	9.61/19.25/28.86	28/ 28/ 28	0.7	3.5	$121 \times 500 \times 5$
55	04:14:52	9.39/18.82/28.21	33/ 33/ 33	0.9	2.7	$121 \times 500 \times 5$
56	04:47:54	9.14/18.31/27.45	38/ 38/ 38	0.8	3.3	$121 \times 500 \times 5$
57	05:22:56	8.82/17.66/26.48	44/ 44/ 44	0.8	3.3	$121 \times 500 \times 5$
58	05:57:25	8.44/16.92/25.36	49/ 49/ 49	0.9	2.8	$121 \times 500 \times 5$
59	06:31:00	8.03/16.08/24.11	54/ 54/ 54	1.0	2.4	$121 \times 500 \times 5$
2013 Dec 09 (UTC) A1-B2-D0						
60	01:03:07	9.16/30.26/34.70	72/ 3/ 17	1.1	2.3	$121 \times 500 \times 5$
61	01:35:54	9.57/30.15/34.48	79/ 9/ 24	1.3	2.0	$121 \times 500 \times 5$
2013 Dec 09 (UTC) A1-C1-D0						
62	02:39:09	15.98/19.78/33.80	57/ 19/ 36	1.0	2.4	$121 \times 500 \times 5$
63	03:57:19	15.70/19.00/32.32	74/ 31/ 50	1.1	2.2	$121 \times 500 \times 5$
64	05:11:02	15.07/17.81/30.12	90/ 42/ 64	0.9	2.6	$121 \times 500 \times 5$
65	06:23:25	14.13/16.17/27.14	107/ 54/ 78	1.0	2.5	$121 \times 500 \times 5$
66	07:33:40	13.04/14.11/23.54	124/ 64/ 93	1.4	1.8	$121 \times 500 \times 5$
67	08:47:08	12.00/11.51/19.41	145/ 76/112	0.7	3.5	$121 \times 500 \times 4$
2013 Dec 10 (UTC) A1-B2-C1						
69	01:01:46	9.19/10.08/15.93	72/ 4/ 36	1.6	1.9	$121 \times 500 \times 5$
70	02:16:17	10.08/ 9.94/15.99	90/ 16/ 53	1.1	2.7	$121 \times 500 \times 5$
71	03:28:54	10.72/ 9.64/15.83	105/ 27/ 69	1.1	2.8	$121 \times 500 \times 5$
72	04:37:36	11.10/ 9.16/15.37	120/ 38/ 83	0.9	3.1	$121 \times 500 \times 5$
73	05:44:27	11.27/ 8.51/14.62	134/ 48/ 98	0.6	4.6	$121 \times 500 \times 5$
74	06:52:38	11.31/ 7.62/13.63	149/ 59/115	0.7	4.0	$121 \times 500 \times 5$
75	08:01:00	11.29/ 6.52/12.56	164/ 69/133	0.9	3.4	$121 \times 500 \times 5$

B. IMAGE RECONSTRUCTION

We started the image reconstruction from the best-fit power-law-type limb-darkened disk in the continuum with the limb-darkened disk diameter of 51 mas and the limb-darkening parameter of 0.6 (Section 3.1). We took advantage of the technique that restores the Fourier phase from the differential phase measurements as described in detail in Ohnaka et al. (2011). While satisfactory images can be reconstructed without a prior or with a flat prior (i.e., constant over the entire field of view of the reconstruction) in the continuum, it is necessary to apply a prior for the image reconstruction in the lines due to the presence of the extended atmosphere and more complex structures. As in our previous works (Ohnaka et al. 2011, 2013, 2017b), a Fermi-function-type prior $Pr(r) = 1/(\exp((r - r_p)/\varepsilon_p) + 1)$ was used, where r is the radius, r_p defines the radius where the function rapidly decreases to 0, and ε_p defines the steepness of the decrease. This function falls off more slowly if ε_p is larger, while it approaches a uniform disk (i.e., it falls off extremely steeply) at the limit of $\varepsilon_p \rightarrow 0$. An example of the radial profile of the prior used in the reconstruction of the images presented in this paper is shown in Figure 9. The Fermi-function-type prior enables us to avoid having strong artifacts spread over the entire field of the reconstruction, while allowing the presence of an extended atmosphere at the same time.

We examined the appropriate ranges of the prior parameters using simulated data. We generated an image of a star consisting of a limb-darkened disk and an extended, circular atmosphere with two spots over the surface and five spots in the atmosphere (Figure 8a). We set the intensity of the extended atmosphere so that the visibility level of the simulated data in the first lobe matches the measurements in the CO lines. The spots over the surface have intensity contrasts of 30% and 15% with respect to the intensity at the stellar disk center. The spots in the atmosphere are characterized with the intensities of 50%, 25%, 17% (two spots with this same intensity), and 12.5% of the intensity at the stellar disk center. However, as Figure 8b shows, after convolving with the same Gaussian beam as used for the observed data, the intensity contrast significantly decreases to 12% (the strongest spot) to 6% (the weakest spot). Interferometric observables (visibility amplitude, closure phase, and Fourier phase) were computed for the same uv coverage as in our AMBER observations with noise comparable to the observed data.

The image reconstruction from the simulated data was carried out with the quadratic (Tikhonov) regularization and the maximum entropy regularization using the above prior. The resulting images were convolved with the same Gaussian beam as used for the observed data. We found that the Fermi-function-type prior with $r_p = 20$ –25 mas and $\varepsilon_p = 2.0$ –3.0 mas is appropriate for the reliable reconstruction of the original simulated image. Figure 8c shows the image reconstructed with $r_p = 22.5$ mas and $\varepsilon_p = 2.5$ mas and the quadratic regularization. The extended atmosphere and the spots are reasonably reproduced, although the outer edge of the atmosphere shows a somewhat irregular shape compared to the original data. If r_p or ε_p is smaller than the above values (i.e., the prior is more compact), the extended atmosphere of the simulated data cannot be well reconstructed.

We then confirmed that the Fermi-function-type prior with the above parameter range allows us to reconstruct images from the R Dor data without producing strong artifacts spread over the field of the reconstruction. We note that the same prior was applied to all 309 spectral channels for a given set of r_p and ε_p . If r_p or ε_p is larger than the above values (i.e., the prior is more extended or falls off more slowly), significant artifacts appear everywhere in the field of the reconstruction. This is also the case if the reconstruction *in the lines* is carried out without a prior or a flat prior (i.e., prior extended over the entire field of the reconstruction). The reason is that the absence of data at baselines even shorter than the shortest baseline of 6.5 m of the present data makes it difficult to reconstruct an extended component.

We used the quadratic (Tikhonov) regularization and the maximum entropy regularization for the image reconstruction from the R Dor data. The image reconstruction was carried out with nine different combinations of the prior parameters with $r_p = 20.0, 22.5$, and 25.0 and $\varepsilon_p = 2.0, 2.5$, and 3.0 using each regularization scheme, resulting in 18 different set-ups in total. We computed the median of the images reconstructed with 18 different set-ups at each wavelength. The spatially resolved spectra over the surface and atmosphere presented in Section 4.2 were extracted from the data cube of these median images.

The image reconstruction with MiRA is carried out by comparing the interferometric observables from the observations and unconvolved images. Therefore, MiRA's output images often have a super-resolution of a factor of 3–5. However, this super-resolution of a factor of 3–5 corresponds to baselines 3–5 times longer than the maximum baseline of the observations. Because we do not have any directly measured information at baselines longer than the actual maximum baseline, the super-resolution images are partially based on extrapolation of Fourier data to longer baselines (to reconstruct structures smaller than the diffraction limit of λ/B_{\max}). Therefore, reconstructed structures smaller

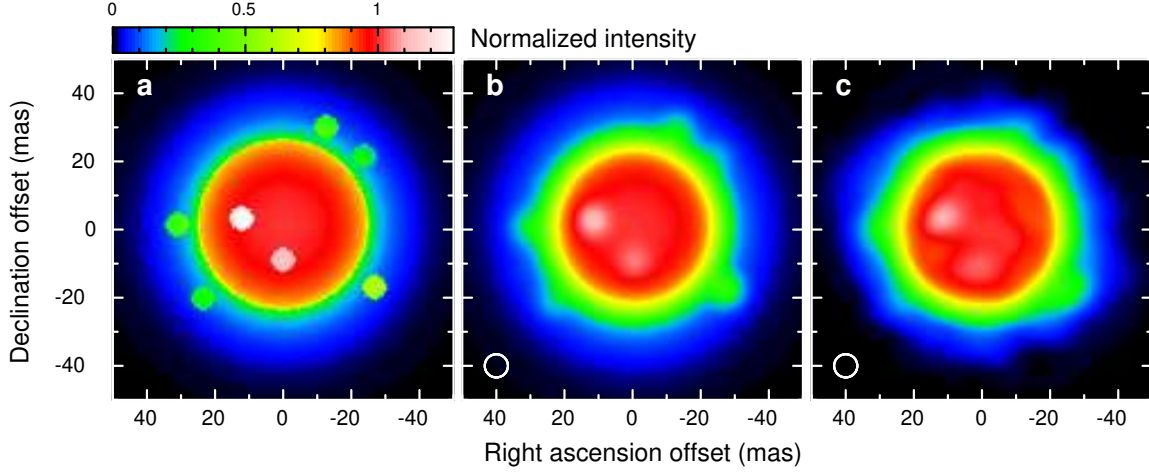


Figure 8. Image reconstruction of simulated data. The images are normalized with the intensity at the stellar disk center (i.e., the intensity higher than 1 means a bright spot). **a:** Original image of the simulated star consisting of a limb-darkened disk, seven spots, and an extended, circular atmosphere. **b:** Image of the simulated star convolved with the same Gaussian beam used for the observed data. **c:** Image reconstructed from the interferometric data generated from the simulated stellar image for the same uv coverage used in the AMBER observations. The reconstruction was carried out in the same manner as for the observed data.

than the diffraction limit of λ/B_{\max} may be real but may also be artifacts. By convolving the MiRA’s super-resolution output image with the Gaussian beam with the FWHM of λ/B_{\max} , the artifacts are suppressed. While we may lose structures that are smaller than the diffraction limit and may be real, we can focus structures resolved with the conservative diffraction-limited resolution.

Figure 9 shows the radial profile of the Fermi-function-type prior with $r_p = 22.5$ mas and $\varepsilon_p = 2.5$ mas and the azimuthally averaged radial profiles of the images reconstructed across the CO line profile centered at $2.30155 \mu\text{m}$ (Figure 4l). The radial profiles were obtained from the reconstructed images not convolved with the Gaussian beam for comparison with the prior. Because the reconstructed images show significant wavelength-dependent surface inhomogeneities, we opted to normalize the radial profiles with the median of the intensity over the stellar disk, instead of normalizing with the maximum intensity. The figure shows that the spatial extension of the atmosphere as well as the surface structures significantly changes across the line profile, although the same, wavelength-independent prior was used. This suggests that the wavelength-dependence of the reconstructed images is not dominated by the prior but it reflects the observed data. Comparisons between the measured interferometric observables and those from the images reconstructed at nine wavelength channels in the lines of Mg, H_2O , and CO (quadratic regularization with $r_p = 22.5$ mas and $\varepsilon_p = 2.5$ mas) are shown in Figures 10 and 11.

To estimate the uncertainty in the line-of-sight velocity measurement, we extracted the velocity-field maps of the Mg, H_2O , and CO lines from each of the data cubes reconstructed with 18 different set-ups described above. Then we obtained maps of the standard deviation of the line-of-sight velocity from the 18 velocity-field maps. The standard deviation of the line-of-sight velocity among the 18 maps is at most 1 km s^{-1} in most parts over the surface and atmosphere. The uncertainty in the systemic velocity is estimated to be 1 km s^{-1} , given the range of $6\text{--}8 \text{ km s}^{-1}$ (in the local standard of rest) obtained from various radio/far-IR observations as discussed in Sect. 3.2. Adding the uncertainty in the wavelength calibration (1.0 km s^{-1}), the total 1σ uncertainty in the velocity measurement is estimated to be 1.7 km s^{-1} . Figures 7d–7f show the maps of the total standard deviation (1σ) including the uncertainty originating from 18 different reconstruction set-ups and the uncertainty in the systemic velocity and the wavelength calibration.

The data files of the interferometric observables used for our image reconstruction are available in the OIFITS format at the Optical interferometry DataBase (OiDB) at the Jean-Marie Mariotti Center (<http://oidb.jmmc.fr/index.html>).

REFERENCES

- Adam, C., & Ohnaka, K. 2019, A&A, in press, astro-ph/1907.05534
- Arenou, F., Grenon, M., & Gómez, A. 1992, A&A, 258, 104

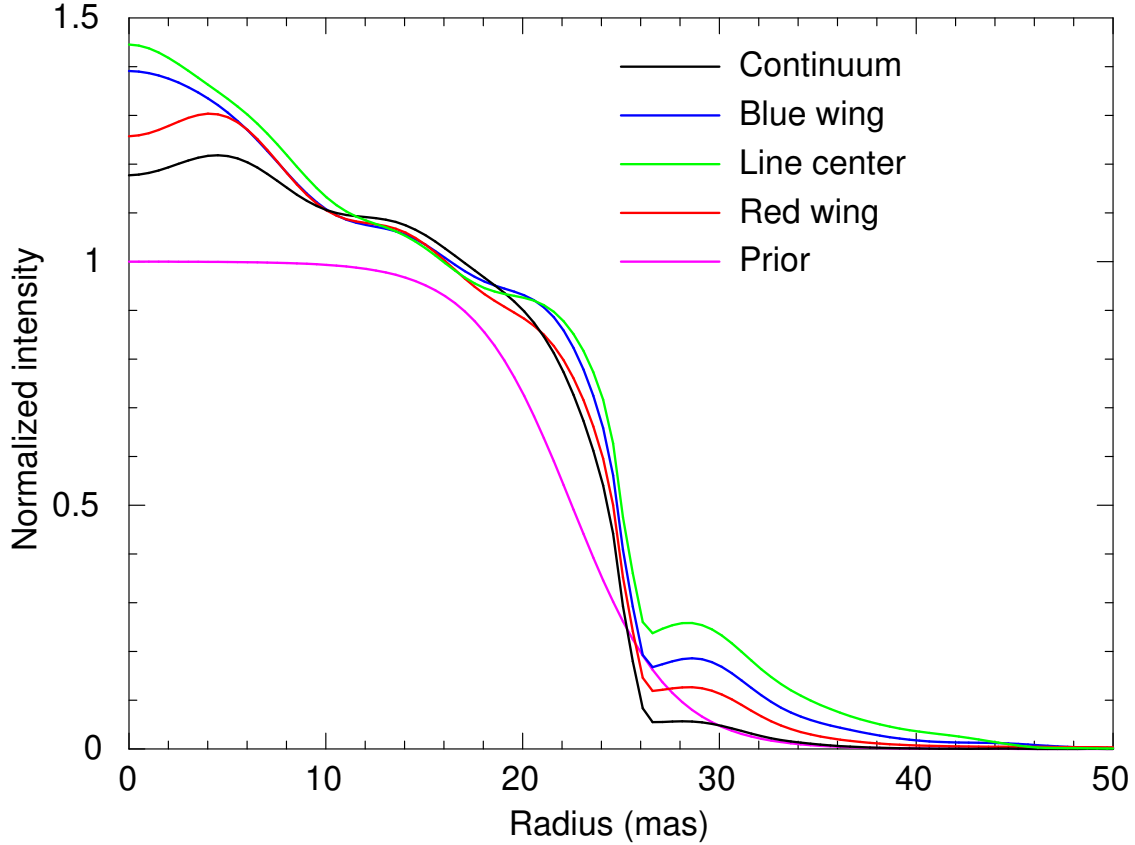


Figure 9. Radial profiles of the prior and the azimuthally averaged radial profiles of the images reconstructed across the CO line profile centered at $2.30155 \mu\text{m}$. The reconstruction was carried out with the quadratic regularization with $r_p = 22.5$ mas and $\varepsilon_p = 2.5$ mas. The radial profiles of the reconstructed images are normalized with the median of the intensity within the star’s limb at each wavelength.

Bedding, T. R., Zijlstra, A. A., von der Lühe, O., et al. 1997, *MNRAS*, 286, 957
 Cardelli, J. A., Clayton, G. C., & Mathis, J. S. 1989, *ApJ*, 345, 245
 Chelli, A., Hernandez Utrera, O., & Duvert, G. 2009, *A&A*, 502, 705
 Decin, L., Richards, A. M. S., Danilovich, T., Homan, W., & Nuth, J. A. 2018, *A&A*, 615, A28
 Deutsch, A. J. 1956, *ApJ*, 123, 210
 Domiciano de Souza, A., Bendjoya, P., Vakili, F., Millour, F., & Petrov, P. G. 2008, *A&A*, 489, L5
 Ducati, J. R. 2002, *Catalogue of Stellar Photometry in Johnson’s 11-color system*
 Efron, B., & Tibshirani, R. J. 1993, *An Introduction to the Bootstrap* (New York, Chapman & Hall)
 Freytag, B., Liljegren, S., & Höfner, S. 2017, *A&A*, 600, A137
 González Delgado, D., Olofsson, H., Kerschbaum, F., et al. 2003, *A&A*, 411, 123
 Goorvitch, D. 1994, *ApJS*, 95, 535

Gustafsson, B., Edvardsson, B., Eriksson, K., et al. 2008, *A&A*, 486, 951
 Hinkle, K. H., & Barnes, T. G. 1979, *ApJ*, 227, 923
 Hinkle, K. H., Lebzelter, T., Joyce, R. R., & Fekel, F. C. 2002, *AJ*, 123, 1002
 Homan, W., Danilovich, T., Decin, L., et al. 2018, *A&A*, 614, A113
 Höfner, S. 2008, *A&A*, 491, L1
 Höfner, S., Bladh, S., Aringer, B., & Ahuja, R. 2016, *A&A*, 594, A108
 Höfner, S., & Olofsson, H. 2018, *A&A Rv*, 26, 1
 Höfner, S., & Freytag, B. 2019, *A&A*, 623, A158
 Hestroffer, D. 1997, *A&A*, 327, 199
 Hillen, M., Verhoelst, T., Degroote, P., Acke, B., & van Winckel, H. 2012, *A&A*, 538, L6
 Ireland, M. J., Tuthill, P. G., Davis, J., & Tango, W. 2005, *MNRAS*, 361, 337
 Jorissen, A., Smith, V. V., & Lambert, D. L. 1992, *A&A*, 261, 164

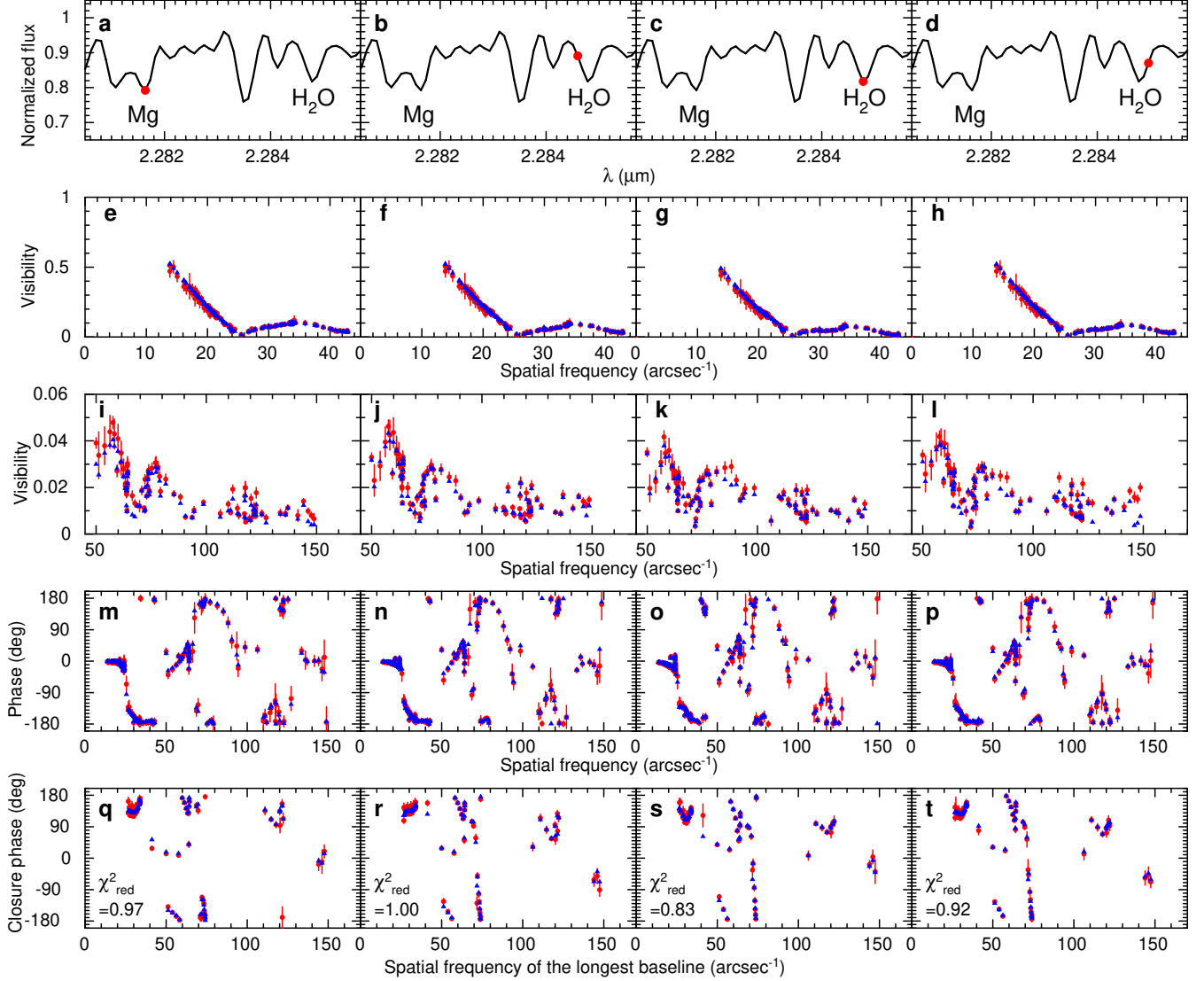


Figure 10. Comparison of the observed interferometric observables and those from the images reconstructed in the Mg ($2.28164 \mu\text{m}$) and H₂O lines ($2.28478 \mu\text{m}$). The reconstruction was carried out with the quadratic regularization with $r_p = 22.5 \text{ mas}$ and $\varepsilon_p = 2.5 \text{ mas}$. The top row (a–d) shows the observed spectrum across the Mg and H₂O lines. The interferometric observables at the wavelength channels marked by the filled circles are shown in the corresponding columns. The second, third, fourth and fifth rows show comparisons of the visibility at spatial frequencies lower than 45 arcsec^{-1} , visibility at spatial frequencies higher than 45 arcsec^{-1} , Fourier phase, and closure phase, respectively. The red dots with the error bars represent the observed data, while the blue triangles represent the values from the reconstructed images. The reduced χ^2 values including the visibilities, Fourier phases and closure phases, are given in the bottom row.

Jørgensen, U. G., Johnson, H. R., & Nordlund, Å 1992, A&A, 261,263
 Khouri, T., Maercker, M., Waters, L. B. F. M., et al. 2016, A&A, 591, A70
 Khouri, T., Vlemmings, W. H. T., Olofsson, H., et al. 2018, A&A, 620, A75
 Kurucz, R. L., & Bell, B. 1995, Atomic Line Data, Kurucz CD-ROM No. 23. Cambridge, Mass.: Smithsonian Astrophysical Observatory

Lacour, S., Thiébaud, E. Perrin, G., et al. 2009, ApJ, 707, 632
 Lagarde, N., Decressin, T., Charbonnel, C. 2012, A&A, 543, A108
 Le Bouquin, J.-B., Absil, O., Benisty, M., et al. 2009, A&A, 498, L41
 Martí-Vidal, I., Marcaide, J. M., Quirrenbach, A., et al. 2011, A&A, 529, A115
 Mermilliod, J. C. 1987, A&AS, 71, 413

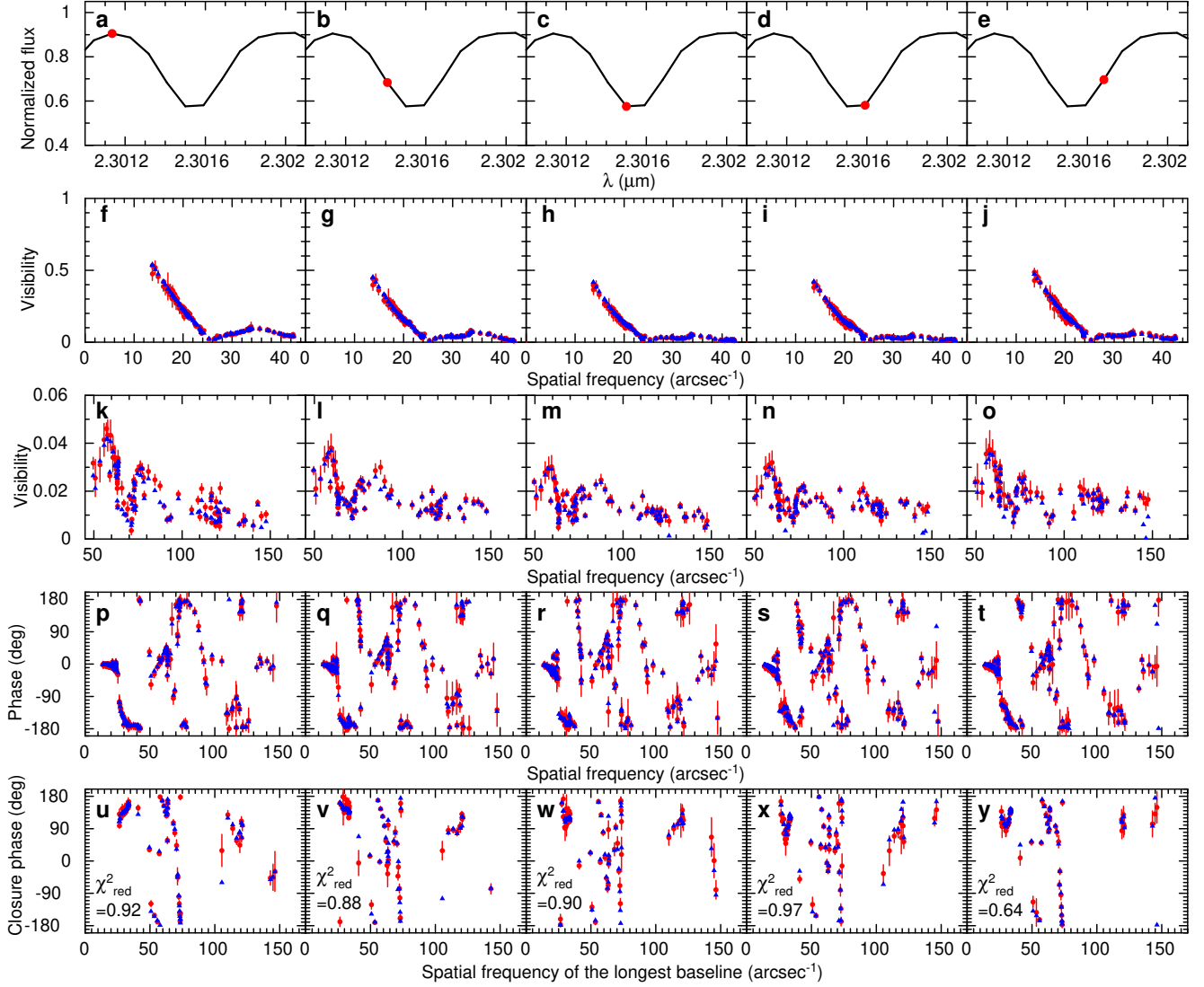


Figure 11. Same as Figure 10 but for the CO line at 2.30150 μm , shown in Figure 4l.

- Millour, F., Meilland, A., Chesneau, O., et al. 2011, *A&A*, 526, A107
- Norris, B. R. M., Tuthill, P. G., Ireland, M. J., et al. 2012, *Nature*, 220, 484
- Ohnaka, K., Hofmann, K.-H., Benisty, M., et al. 2009, *A&A*, 503, 183
- Ohnaka, K., Weigelt, G., Millour, F., et al. 2011, *A&A*, 529, A163
- Ohnaka, K., Hofmann, K.-H., Schertl, D., et al. 2012, *A&A*, 537, A53
- Ohnaka, K., Hofmann, K.-H., Schertl, D., et al. 2013, *A&A*, 555, A24
- Ohnaka, K., Weigelt, G., Hofmann, K.-H. 2016, *A&A*, 589, A91
- Ohnaka, K., Weigelt, G., Hofmann, K.-H. 2017, *A&A*, 597, A20
- Ohnaka, K., Weigelt, G., Hofmann, K.-H. 2017, *Nature*, 310, 548
- Ohnaka, K., Hadjara, M., & Maluenda Berna, M. Y. L. 2019, *A&A*, 621, A6
- Paladini, C., Baron, F., Jorissen, A., et al. 2018, *Nature*, 310, 553
- Park, S., et al. 2018, *ApJ*, 238, 29
- Petrov, R. G., Malbet, F., Weigelt, G., et al. 2007, *A&A*, 464, 1
- Polyansky, O. L., Kyuberis, A. A., Zobov, N. F. 2018, *MNRAS*, 480, 2597
- Price, S. D., Smith, B. J., Kuchar, T. A., Mizuno, D. R., & Kraemer, K. E. 2010, *ApJS*, 190, 203

- Ragland, S., Le Coroller, H., Pluzhnik, E., et al. 2008, *ApJ*, 679, 746
- Ryde, N., & Eriksson, K. 2002, *A&A*, 386, 874
- Samus, N. N., Kazarovets, E. V., Durlevich, O. V., Kireeva, N. N., Pastukhova, E. N., General Catalogue of Variable Stars: Version GCVS 5.1, 2017, *Astronomy Reports*, 2017, 61, 80
- Schmitt, H. R., Pauls, T. A., Tycner, C., et al. 2009, *ApJ*, 691, 984
- Sloan, G. C., Kraemer, K. E., Price, S. D., & Shipman, R. F. 2003, *ApJS*, 147, 379
- Snedden, C., Lucatello, S., Ram, R. S., Brooke, J. S. A., & Bernath, P. 2014, *ApJS*, 214, 26
- Stewart, P. N., Tuthill, P. G., Nicholson, P. D., Sloan, G. C., & Hedman, M. M. 2015, *ApJS*, 221, 30
- Tatulli, E., Millour, F., Chelli, A., et al. 2007, *A&A*, 464, 29
- Thiébaud, E. 2008, *Proc. SPIE*, 7013, 70131I
- Van de Sande, M., Decin, L., Lombaert, R., et al. 2018, *A&A*, 609, A63
- van Leeuwen, F. 1997, *A&A*, 474, 653
- Vlemmings, W. H. T., Khouri, T., De Beck, E., et al. 2018, *A&A*, 613, L4
- Weigelt, G., Hofmann, K.-H., Schertl, D., et al. 2016, *A&A*, 594, A106
- Wittkowski, M., Boboltz, D. A., Driebe, T., et al. 2008, *A&A*, 479, L21
- Wittkowski, M., Boboltz, D. A., Ireland, M., et al. 2011, *A&A*, 532, L7
- Wittkowski, M., Hofmann, K.-H., Höfner, S., et al. 2017, *A&A*, 601, A3